Electronic Supplementary Material (ESI) for Nanoscale.

SUPPORTING INFORMATION

Microporous carbon nanosheets with redox-active heteroatoms for pseudocapacitive charge storage

Young Soo Yun, Do-Hoon Kim, Sung Ju Hong, Min Hong Park, Yung Woo Park, Byoung Hoon Kim, Hyoung-Joon Jin, and Kisuk Kang**

[1]*Department of Materials Science and Engineering, Seoul National University, Seoul 151-742, Korea*

[2]*Department of Physics and Astronomy, Seoul National University, Seoul 151-747, Korea*

[3]*Department of Polymer Science and Engineering, Inha University, Incheon 402-751, Korea*

[4]*Department of Physics, Incheon National University, Incheon 406-772, Korea*

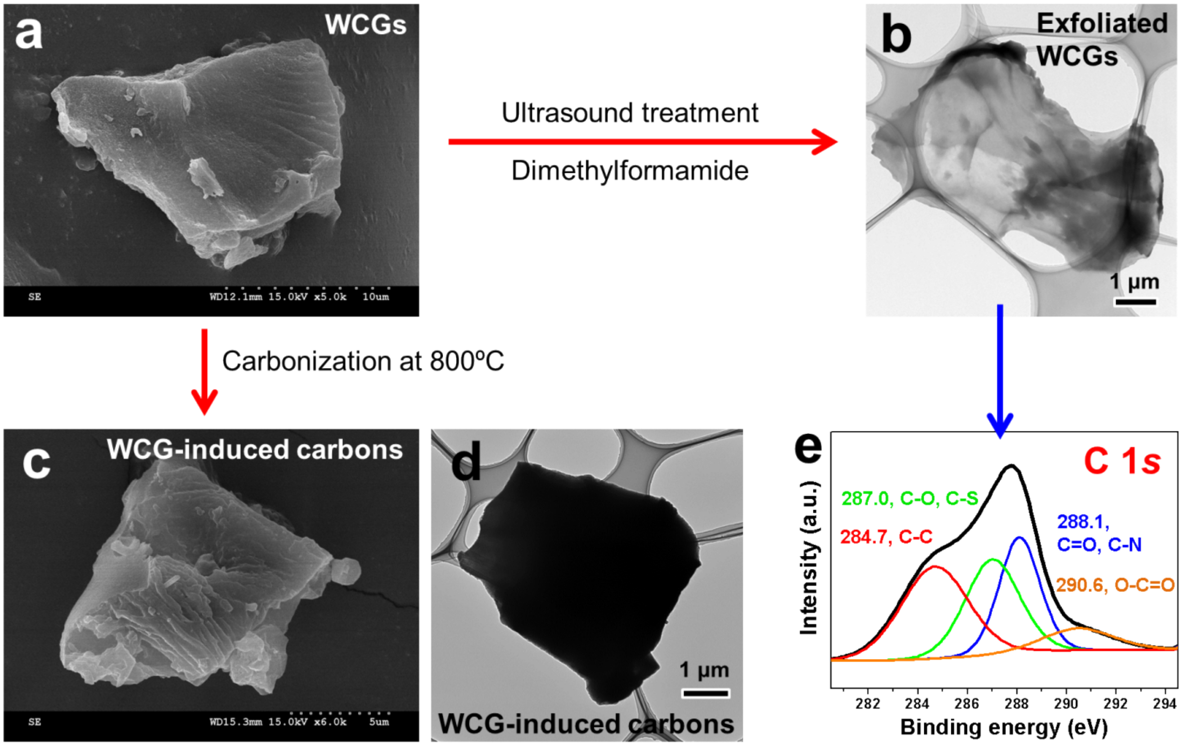

Figure S1. (a) FE-SEM image of the WCGs. (b) FE-TEM image of exfoliated WCGs. (c) FE-SEM image and (d) FE-TEM image of WCG-induced carbons. (e) XPS C 1s spectra of exfoliated WCGs.

Micrometre-scale WCG particles were exfoliated by ultrasound treatment in dimethylformamide solution [Fig. S1(a)]. The exfoliated WCGs were composed of various chemical species containing oxygen, nitrogen and sulphur heteroatoms [Fig. S1(b)]. XPS C 1s spectra of the exfoliated WCGs showed s several distinct peaks related to the C-C bond (284.7 eV), C=O and C-N bonds (288.1 eV), and the O−C=O bond (290.6 eV) containing C−O and C−S bonding centred at 287.0 eV [Fig. S1(e)]. In contrast, WCG-induced carbons fabricated with no activation agent, KOH, showed bulk morphologies with micrometre-scale size [Figs. S1(c), (d)].

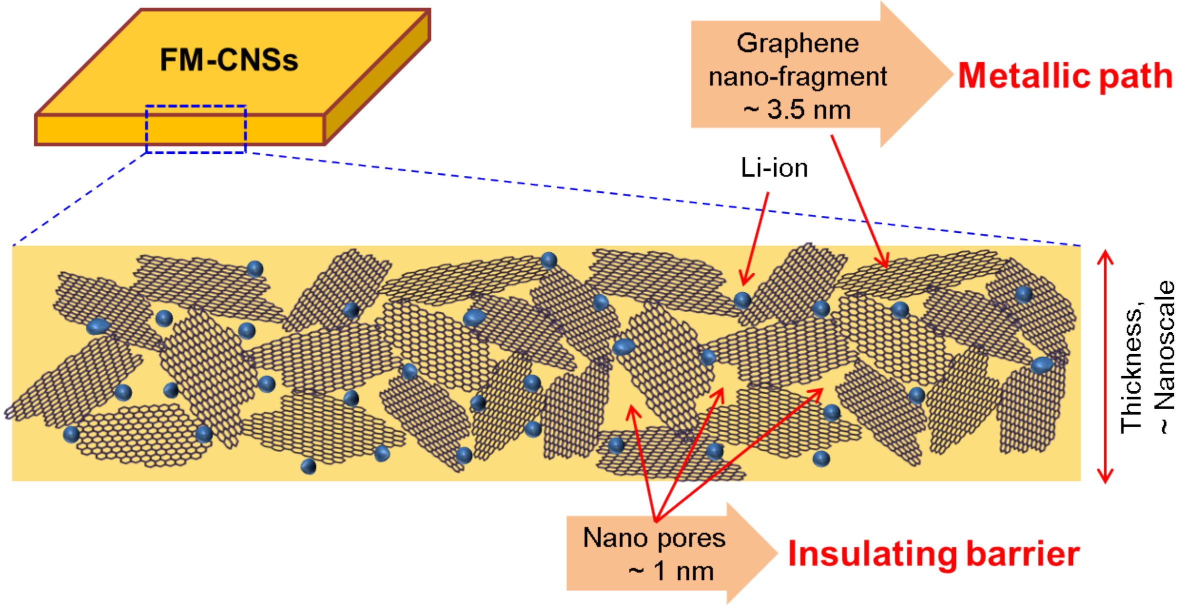

Figure S2. Schematic image of the FM-CNS microstructure.

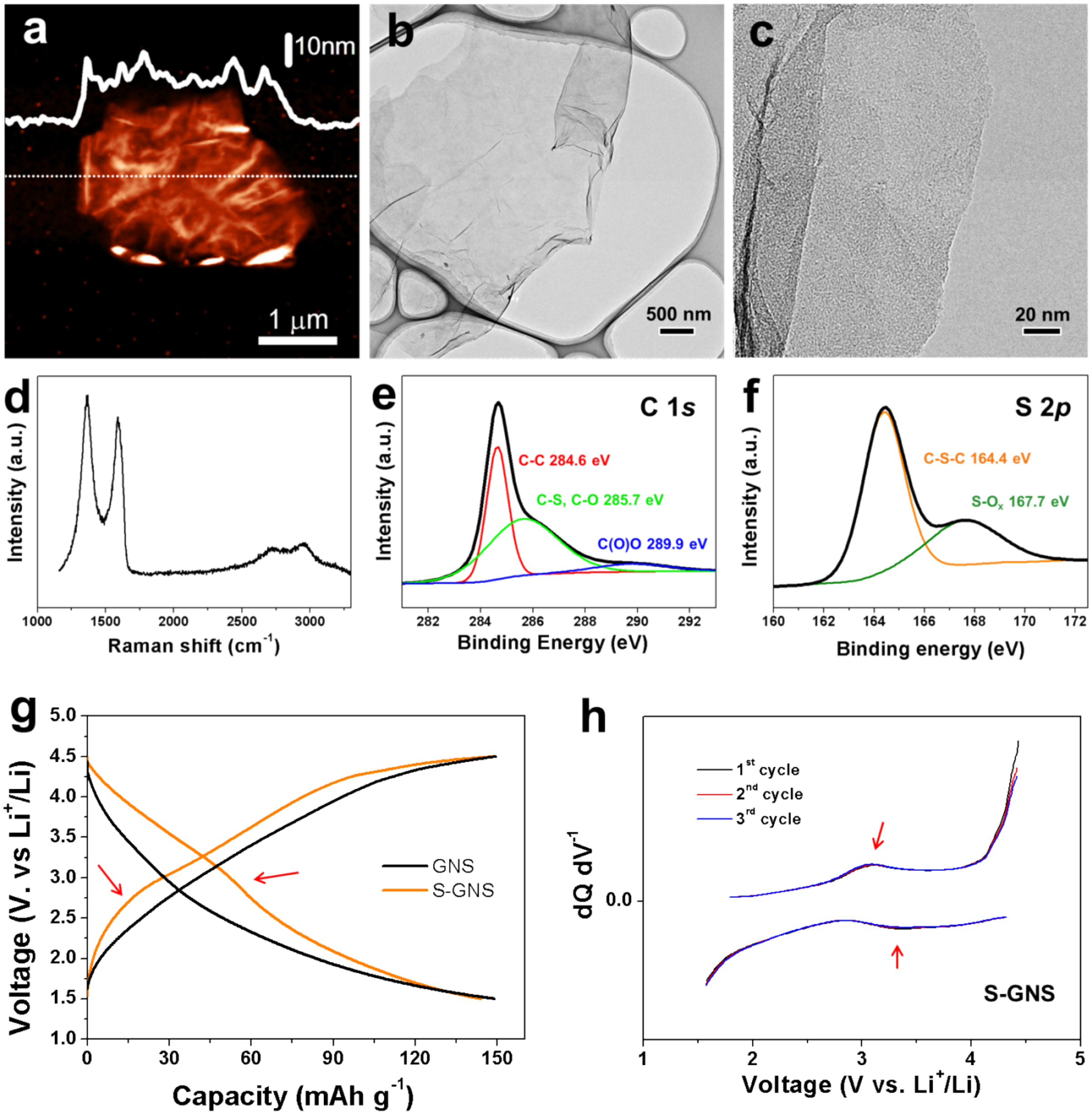

Figure S3. Morphologies of S-GNSs observed by (a) AFM and (b),(c) FE-TEM imaging at the indicated magnifications. (d) Raman spectrum of S-GNSs. XPS (e) C 1*s* and (f) S 2*p* spectra of S-GNSs. (g) Galvanostatic charge/discharge profiles of GNSs and S-GNSs in a potential range of 1.5 to 4.5 at a current density of 0.2 A g^{-1}. (h) dQ/dV plots based on the charge/discharge profiles of S-GNSs.

S-GNSs and GNSs were prepared using the method described in reference 8. Characteristics of the GNSs are described in Fig. S5. The S-GNSs had a ~10 nm thickness and lateral sizes of several micrometres [Fig. S3(a−c)]. Raman spectra of S-GNSs exhibited *D*−,*G*− and 2*D*-peak frequencies, which were, respectively, ~ 1366, 1590 and 2723 cm^{-1} [Fig. S3(d)]. The I_D/I_G ratio (*D*-peak intensity: *G*-peak intensity) in S-GNS was ~ 0.88, which means that the S-GNSs have an amorphous carbon structure with nanometre-scale graphitic domains. XPS C 1s spectrum of S-GNSs exhibited C−S, C−N bonding centred at 285.7 eV and C(O)O bonding centred at 289.9 eV containing a main C−C bonding centred at 284.6 eV. Also, XPS S 2 *p* spectrum clearly showed the presence of C−S−C bonding and $\mathrm{C{-}SO_x}$ bonding centred at 164.4 and 167.7 eV, respectively.

Galvanostatic charge/discharge profiles of GNSs and S-GNS showed a clear difference in the potential range 1.5 to 4.5 V [Fig. S3(g)]. The profile of S-GNSs had a higher average potential in charge/discharge, and an additional redox reaction at around 3 V was observed. The dQ/dV curves of S-GNSs confirm the reversible redox reactions [Fig. S3(h)]. In addition, the reversibility capacities of GNSs and S-GNSs were similar, although GNSs have larger oxygen contents (16.5 at.%) than S-GNSs (12.1 at.%). Considering the sulphur content of 4.2 at.% in S-GNSs, this result could be attributed to sulphur groups in S-GNSs contributing to an enhancement of the specific capacity. Thus, these results suggest that sulphur-functional groups in carbon structures can be a redox active site for pseudocapacitive lithium-ion storage.

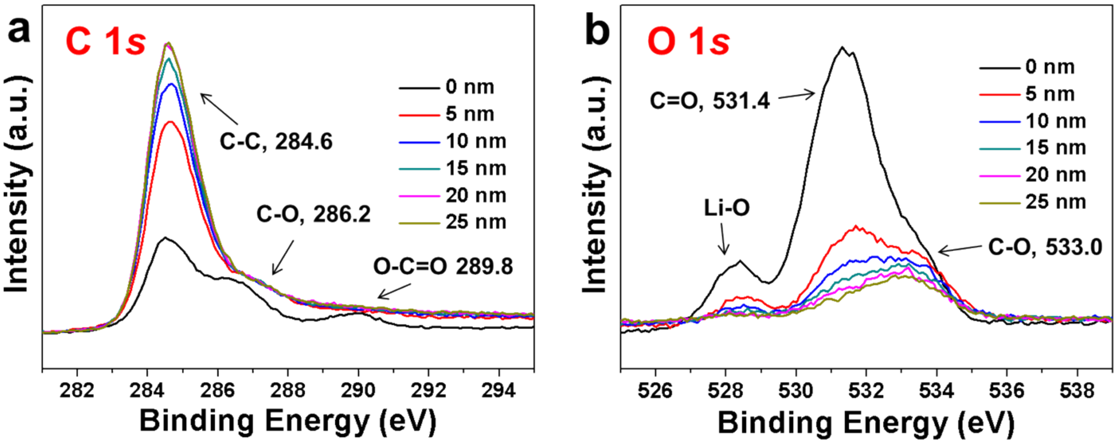

Figure S4. Ex-situ XPS spectra of the FM-CNS electrode after 10 charge/discharge cycles.

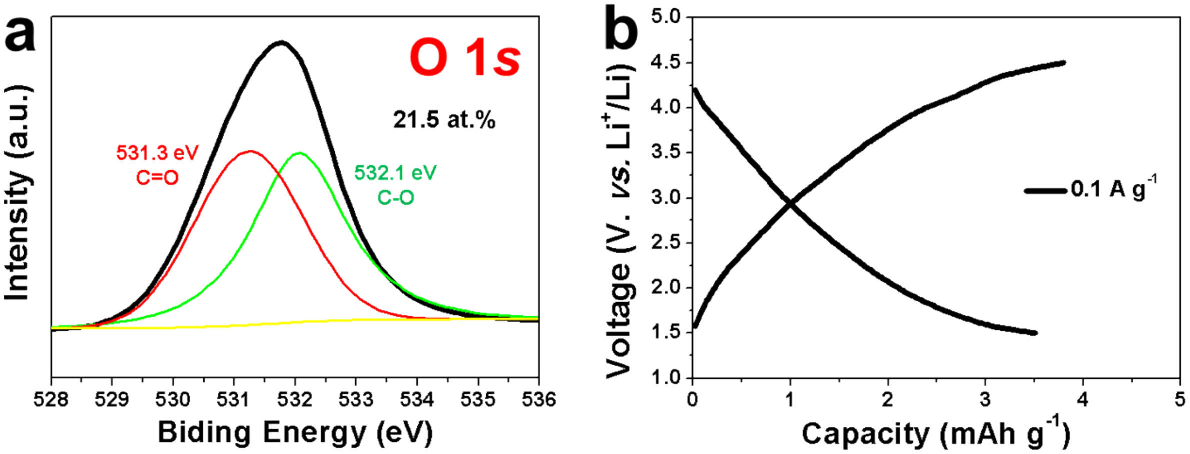

Figure S5. (a) XPS O 1s spectrum and (b) galvanostatic charge/discharge profiles of WCG-induced carbons with no activation agents.

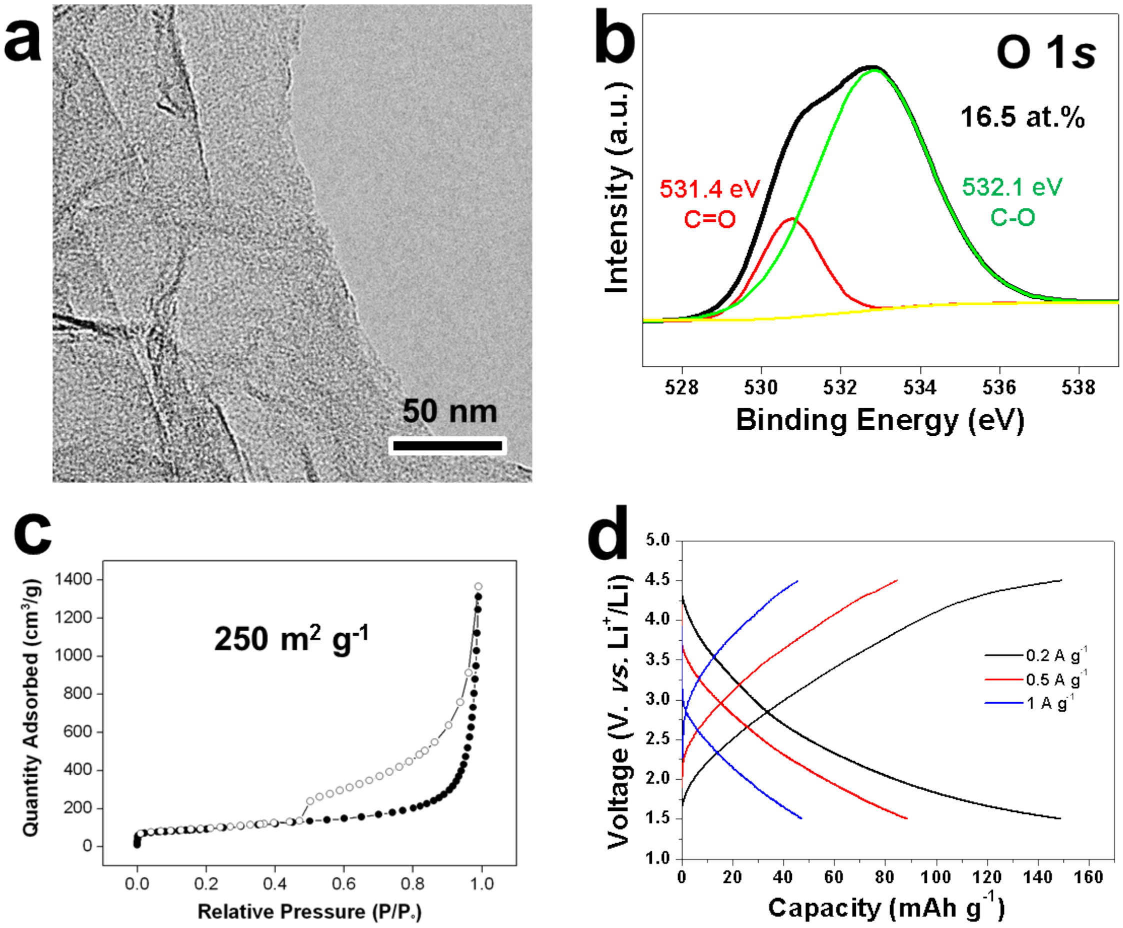

Figure S6. (a) FE-TEM image and (b) XPS O 1s spectrum of GNSs. (c) Nitrogen adsorption and desorption isotherm curve of GNSs. (d) Galvanostatic charge/discharge profiles of GNSs at a different current density of 0.2, 0.5 and 1 A g^{-1}.

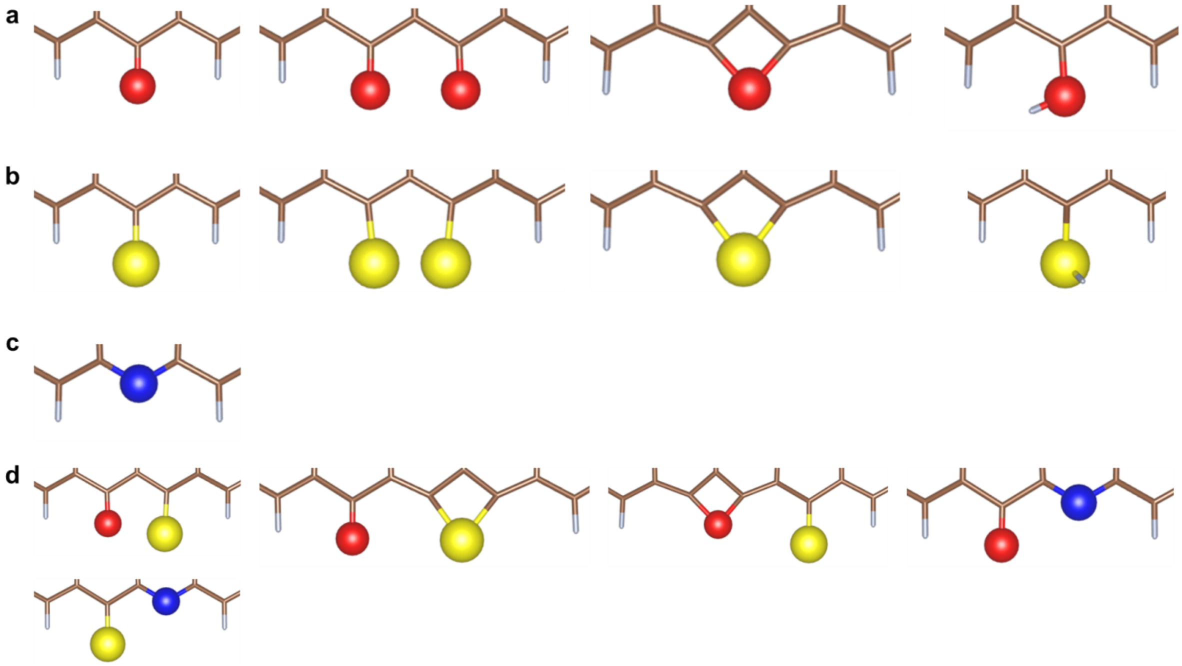

Figure S7. Various configurations of (a) oxygen atoms, (b) sulphur atoms, (c) nitrogen atom and (d) their combinations (brown, carbon; grey, hydrogen; red, oxygen; yellow, sulphur; blue, nitrogen) in graphene nanoribbon.

Table S1. Bader charge analysis for neighbouring two heteroatoms such as oxygen-oxygen (O-O), oxygen-sulphur (O-S), oxygen-nitrogen (O-N) and sulphur-nitrogen (S-N) with lithium ion.

Heteroatoms	O	S	N	Li
O-O	7.15, 7.14	None	None	0.13
O-S	7.22	6.39	None	0.1
O-N	7.15	None	6.27	0.1
S-N	None	6.34	6.28	0.13

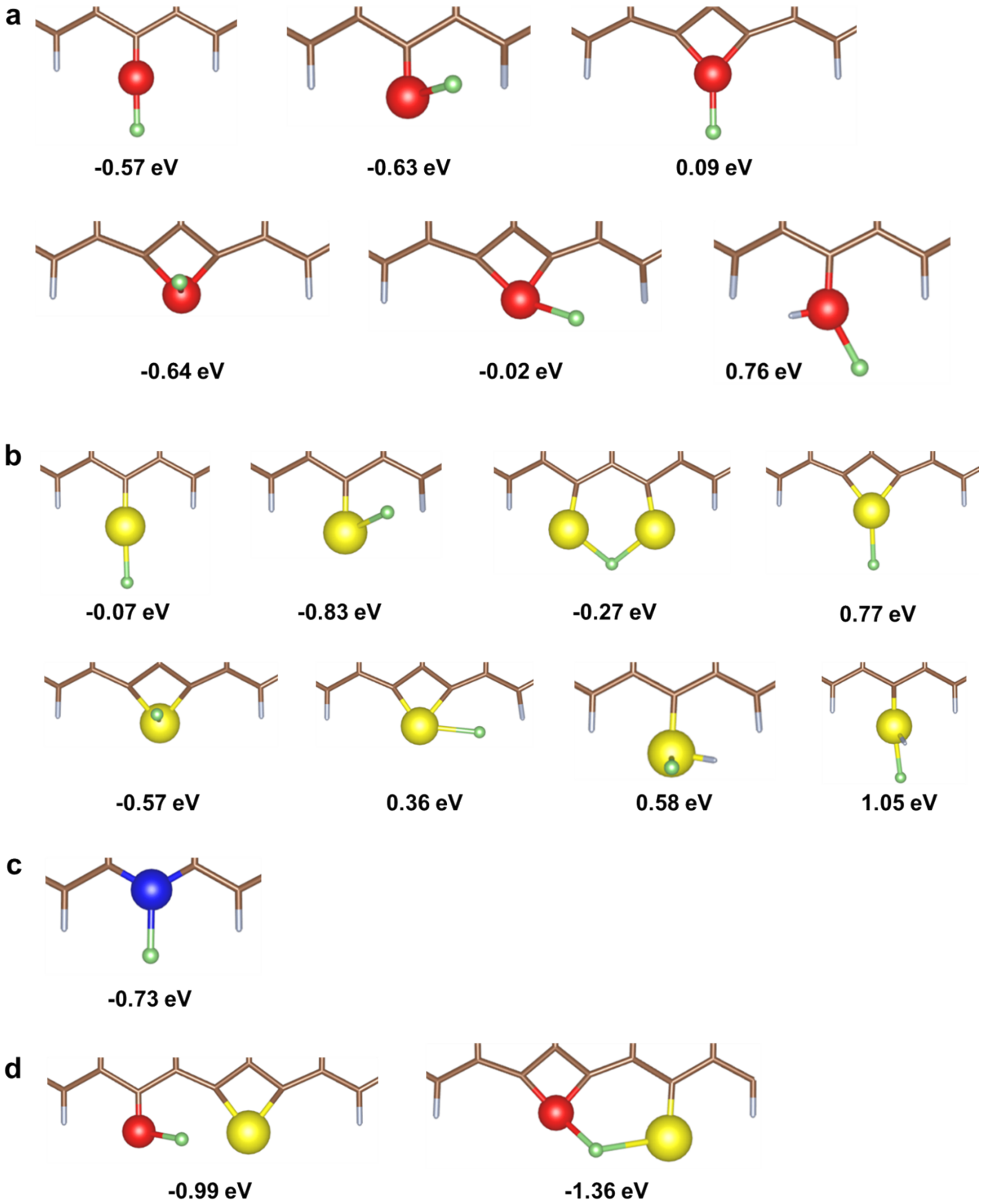

Figure S8. Configurations of (a) oxygen atoms, (b) sulphur atoms, (c) nitrogen atom and (d) oxygen-sulphur combinations with lithium ion (brown, carbon; grey, hydrogen; red, oxygen; yellow, sulphur; blue, nitrogen; green, lithium).

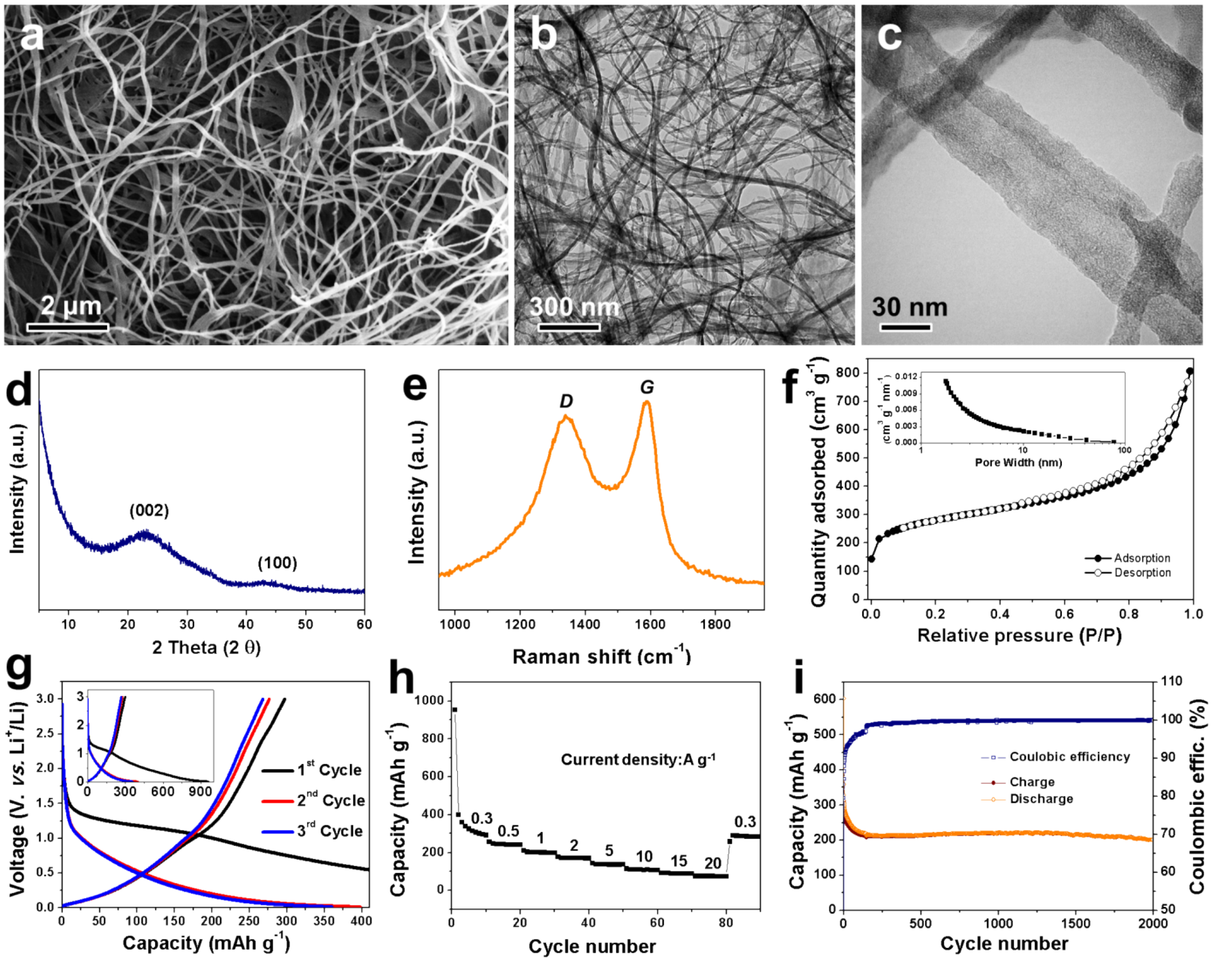

Figure S9. Morphologies of HP-CNFs observed by (a) FE-SEM image and (b),(c) FE-TEM images with different magnifications. (d) XRD data and (e) Raman spectrum of HP-CNFs. (f) Nitrogen adsorption and desorption isotherm curve and inset is pore size distribution of HP-CNFs. (g) Galvanostatic charge/discharge profiles of HP-CNFs in a potential window of 0.01 to 3 V at a current density of 0.3 A g^{-1}. (h) Rate capabilities of HP-CNFs at a various current densities from 0.3 A g^{-1} to 20 A g^{-1}. (i) Cycling performance of HP-CNFs for 2000 cycles at a current density of 1 A g^{-1}.

The characteristics of HP-CNFs were as shown in Fig. S9. The ~ 50-nm thickness nanofibres are loosely entangled, leading to a macroporous structure [Fig. S9(a-c)]. The broad graphitic (*002*) and (*100*) peaks in XRD pattern of HP-CNFs mean that the carbon structure of HP-CNFs is amorphous [Fig. S9(d)], and the *D* and *G* bands (I_D/I_G intensity ratio of ~ 0.9) in Raman spectra show the presence of a nanometre-size hexagonal carbon structure [See Fig. 3(e)]; thus, the carbon structure of HP-CNFs is composed of several nanometre-sized graphitic crystal domains with random orientation. The isotherm curves of HP-CNFs characterised by the nitrogen adsorption and desorption experiments show the hybrid IUPAC Type−I and Type−IV shapes, indicating the existence of domains with microporous and mesoporous structures [Fig. S9(f)]. Pores of the HP-CNFs have a broad distribution ranged by ~ 100 nm, as shown in inset of Fig. S9(f). The BET specific surface area of HP-CNFs was 985.5 m^2 g^{-1}.

Galvanostatic discharge/charge profiles of HP-CNFs showed a linear voltage drop/increase with no distinct plateau, suggesting that HP-CNFs had electrochemically and geometrically nonequivalent Li ion sites [Fig. S9(g)]. The first reversible capacity of HP-CNFs was 298 mAh g^{-1}, which corresponds to $LiC_{7.5}$. Rate capabilities of HP-CNFs from 0.3 to 20 A g^{-1} are shown in Fig S9(h). Highly stable capacities of c.a. 77 mAh g^{-1} can still be obtained at a rate of 20 A g^{-1}. In addition, when the current density returns to 0.3 A g^{-1} after 80 cycles, HP-CNFs successfully recovers its initial capacity, demonstrating good reversibility. The cycling stability of HP-CNFs was tested for 2000 cycles with nearly 100% Coulombic efficiency in all of the discharge/charge cycles at a current density of 1 A g^{-1}.

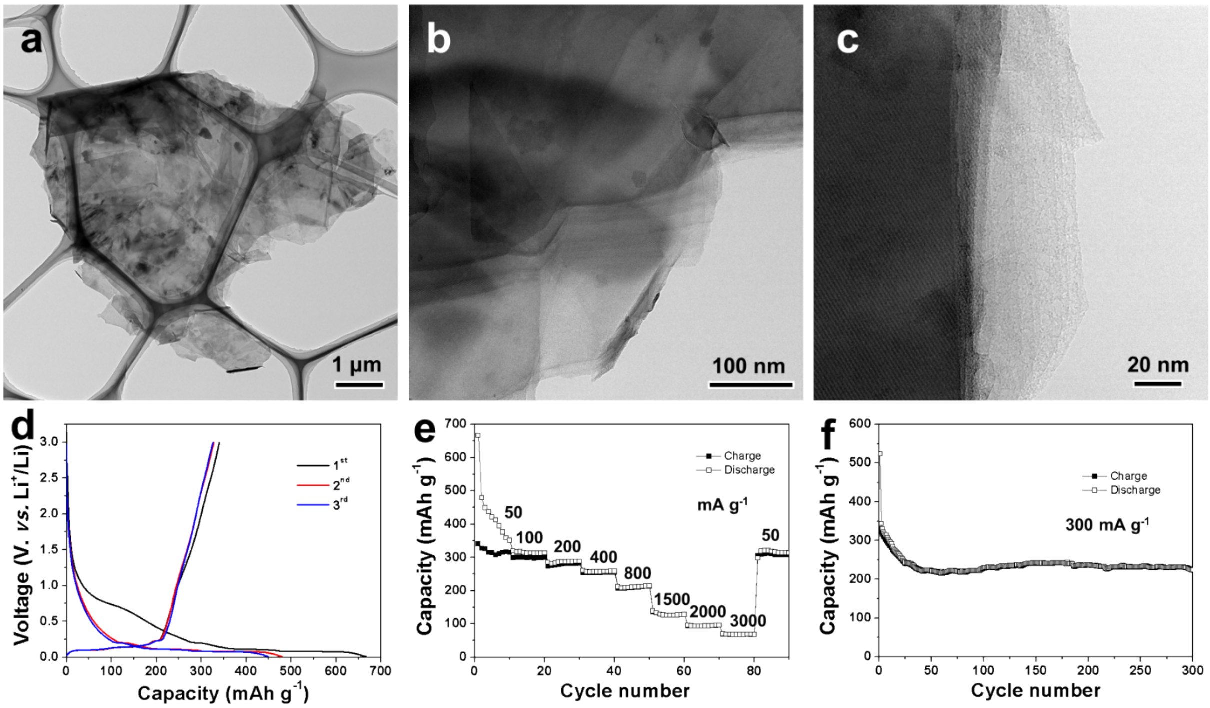

Figure S10. Morphologies of GNPs observed by (a-c) FE-TEM imaging at the indicated magnifications. (d) Galvanostatic discharge/charge profiles at a current rate of 50 mA g^{-1} and (e) rate performances of CNPs. (f) Cyclic performances during 300 cycles at a current density of 300 mA g^{-1}.

FE-TEM images of GNPs show the 2D-like plate shapes with high crystallinity [Fig. S10(a-c)]. Galvanostatic discharge/charge profiles of GNPs show that the lithium-ion storage behaviours of GNPs are composed of two different reaction mechanisms [Fig. S10(d)]. The linear voltage drop/increase of the discharge/charge profiles indicate pseudocapacitive lithium-ion storages on their surface and the plateau at 0.1 V means lithium-ion storage by intercalation in graphitic layers. The nanostructure of GNPs led to high rate capabilities and reversibility, and good cyclic performance over 300 charge/discharge cycles [Fig. S10(e) and (f)].

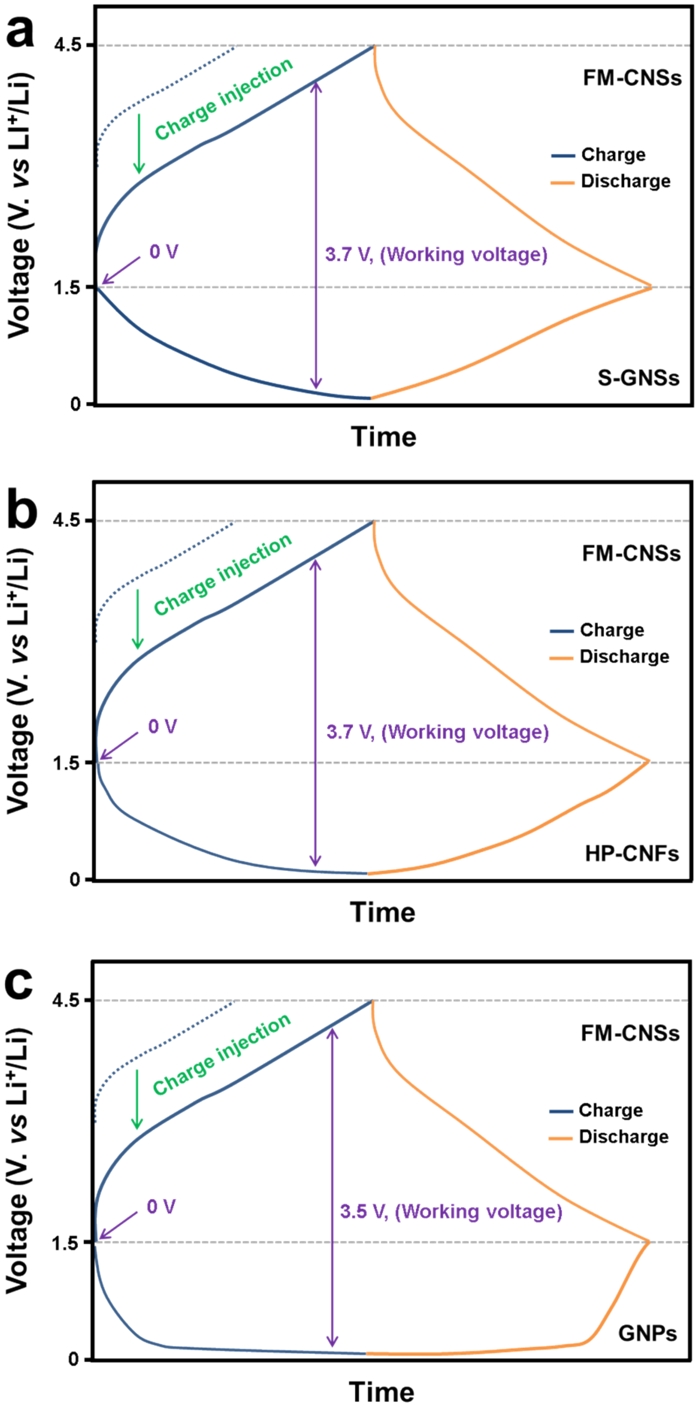

Figure S11. A schematic diagram illustrating the galvanostatic charge/discharge behaviours of asymmetric lithium-ion pseudocapacitors based on (a) S-GNS//FM-CNS, (b) HP-CNF//FM-CNS and (c) GNP//FM-CNS.

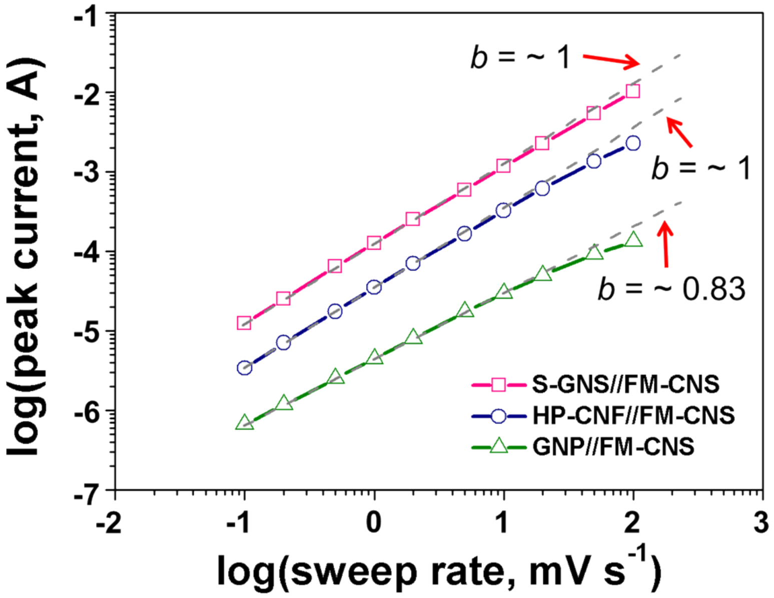

Figure S12. Voltammetric current dependence on the sweep rate.

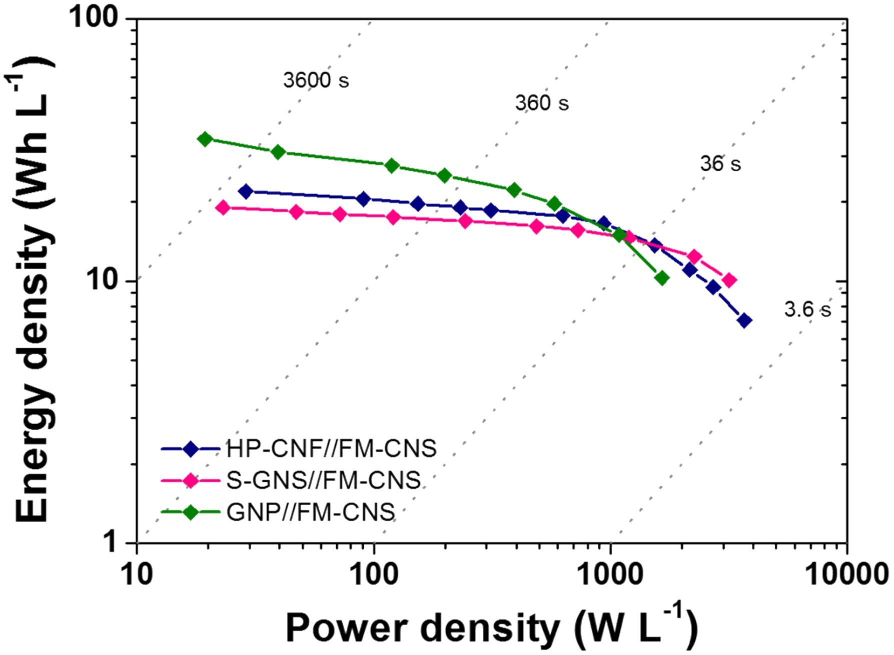

Figure S13. Volumetric power density versus volumetric energy density plots of the GNP//FM-CNS, S-GNS//FM-CNS and HP-CNF//FM-CNS pseudocapacitors.

The tapping density of FM-CNSs was ~0.13 g cm^{-3}, which was calculated by filling a calibrated cylinder with a known sample weight and tapping the cylinder until a minimum volume was recorded. Also, the tapping densities of GNP, S-GNSs and HP-CNFs were calculated as ~0.15, ~0.08 and ~0.11 g cm^{-3}, respectively. Considering the MP ratio of the electrode pairs, the overall tapping densities of GNP//FM-CNS, S-GNS//FM-CNS and HP-CNFs//FM-CNS pseudocapacitors are calculated as ~0.14, ~0.10 and ~0.12 g cm^{-3}, respectively. Therefore, for GNP//FM-CNS pseudocapacitors, specific energy of 248 Wh kg^{-1} at a specific power of 139 W kg^{-1} corresponds to volumetric energy of about 34.7 Wh L^{-1} at a volumetric power of about 19.5 W L^{-1}. Also, the Ragone plot of S-GNS//FM-CNS pseudocapacitors shows a volumetric power density of 3165 W L^{-1} at an energy density of 10 Wh L^{-1}.

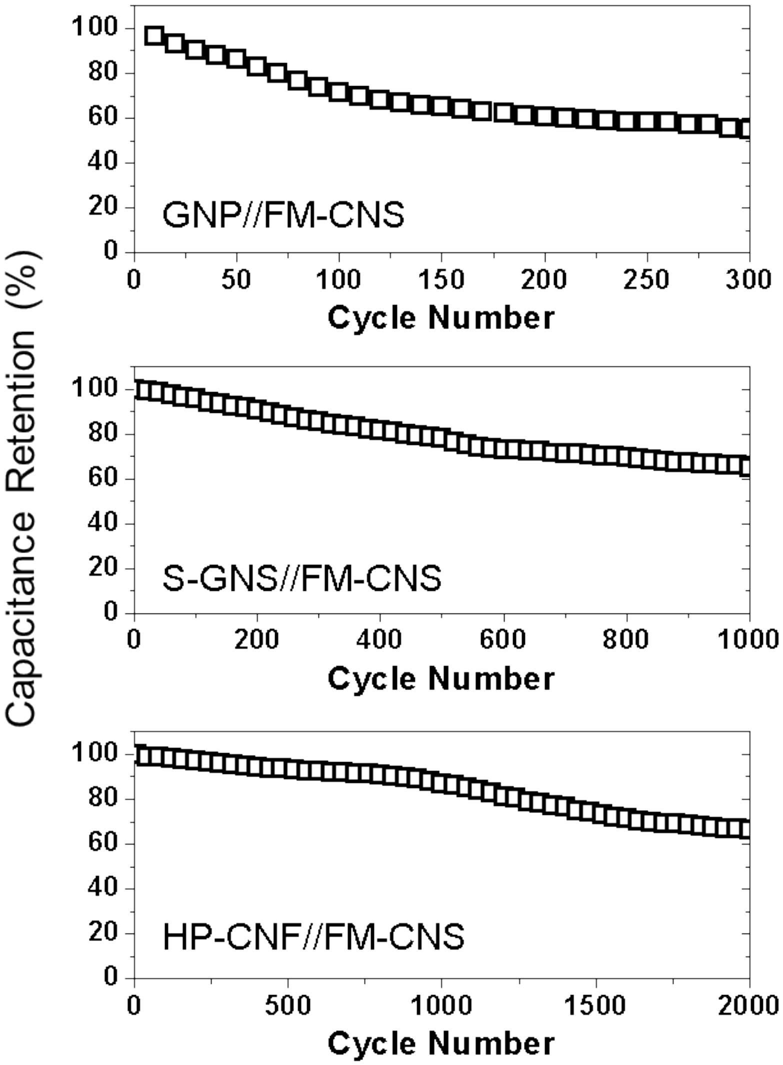

Figure S14. Capacitance retentions of asymmetric lithium-ion pseudocapacitors based on GNP//FM-CNS, S-GNS//FM-CNS and HP-CNF//FM-CNS at current densities of 0.1, 0.3 and 0.3 A g^{-1} over repetitive 300, 1000 and 2000 charge/discharge cycles, respectively.